energies

MDPI

Article

Frequency-Splitting-Free Synchronous Tuning of Close-Coupling Self-Oscillating Wireless Power Transfer

Po Hu *, Jieshuai Ren and Wenan Li

School of Electrical Engineering, Wuhan University, 299 Bayi Road, Wuchang, Wuhan 430072, China; 2011202070070@whu.edu.cn (J.R.); wenanli@whu.edu.cn (W.L.)
* Correspondence: phu@whu.edu.cn; Tel.: +86-153-4221-2426; Fax: +86-27-6252-7627

Academic Editor: Hongjian Sun
Received: 1 May 2016; Accepted: 20 June 2016; Published: 27 June 2016

Abstract: The synchronous tuning of the self-oscillating wireless power transfer (WPT) in a close-coupling condition is studied in this paper. The Hamel locus is applied to predict the self-oscillating points in the WPT system. In order to make the system operate stably at the most efficient point, which is the middle resonant point when there are middle resonant and split frequency points caused by frequency-splitting, the receiver (RX) rather than the transmitter (TX) current is chosen as the self-oscillating feedback variable. The automatic delay compensation is put forward to eliminate the influence of the intrinsic delay on frequency tuning for changeable parameters. In addition, the automatic circuit parameter tuning based on the phase difference is proposed to realize the synchronous tuning of frequency and circuit parameters. The experiments verified that the synchronous tuning proposed in this paper is effective, fully automatic, and more robust than the previous self-oscillating WPT system which use the TX current as the feedback variable.

Keywords: wireless power transfer (WPT); close coupling; self-oscillation; Hamel locus; frequency-splitting; synchronous tuning

1. Introduction

Recently, the magnetic coupling resonant WPT has found widespread applications, such as wireless sensors, electrical vehicles, and wireless household appliances [1–4]. This type of WPT system is non-radiative with ignorable radiative loss [5], and often operates in the close-coupling condition where the transfer range is approximately equal to the diameter of the coils. Therefore, the transfer efficiency is not only high, but also remains nearly unchanged in a certain range even when the gap and misalignment varies [1,3,6]. In order to satisfy the condition of close-coupling, the operating frequency is often set to several kHz–several MHz, and the quality-factor (Q) should be as high as 200–2000 [3,5,7,8]. However, many factors, e.g., environmental changes, aging of the resonant tanks, and errors of individual components of mass production, may lead to variations of the operating frequency or circuit parameters including the inductances and the capacitances, which result in severe detuning in the high-Q resonant tanks [8–10]. To solve these problems, the automatic synchronous tuning method considering the frequency tuning and circuit parameter tuning, i.e., the tuning of the circuit parameters such as capacitances and inductances, should be investigated. The former makes the inverter operate in zero-current switching, and the latter ensures the resonant frequency of the transmitter (TX) and receiver (RX) is the same.

Much of the previous research in this area of WPT focuses on the one-off tuning methods rather than the fully-automatic tuning which keeps the system resonant all the time, shown in Figure 1a,b, respectively. For the frequency tuning, the methods based on frequency-scanning are often used [1,2,6].

The tuning stops when the resonant frequency is found, so the detuning detection and restart control are needed when the tuning stops. In addition, power is not normally transferred in the tuning process. Many of the circuit parameter tuning methods are also one-off tuning or dynamically-stable tuning, such as the disturbance observation method and the intelligent circuit parameter searching method coming from the automatic impedance matching [6,8,11,12].

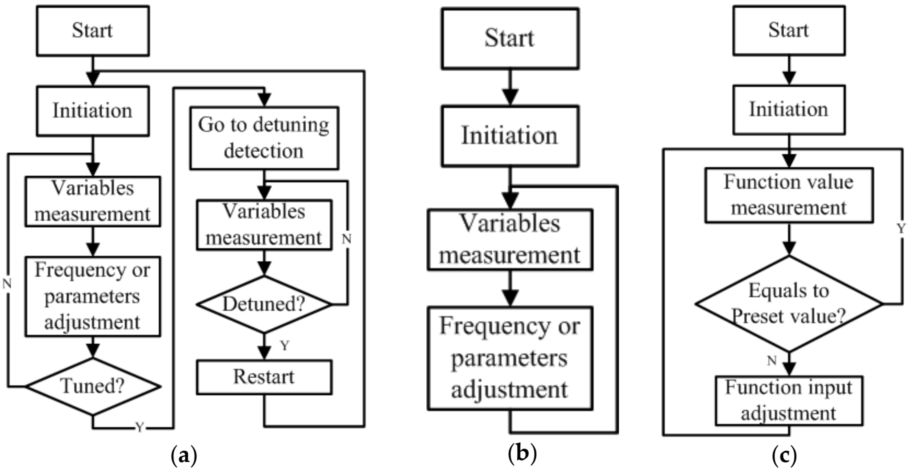

Figure 1. Flowcharts of tuning methods: (**a**) one-off tuning with restart when detuned; (**b**) fully-automatic tuning; and (**c**) tuning according to functions.

The fully automatic frequency or circuit parameter tuning is also studied before. The frequency control by detecting the detuning loop current in inverter [9,13] is complex, and cannot be used in high-power applications for long. The circuit parameters setting, based on the function between the measurement and the control variable, is precise and easily conducted, as shown in Figure 1c, but some of these methods are based on table or online circuit parameter calculations [6,14,15], and the precise measurement of the circuit parameter values, which must be obtained in advance, are uncertain or changeable in applications. In addition, the previous circuit parameter tuning is not always effective for the variable frequency caused by automatic frequency tuning.

The self-oscillating control method makes the inverter flip at the moment when the TX current crosses zero, so the operating frequency of the inverter, i.e., the self-oscillating frequency, equals to the resonant frequency even if circuit parameters change [13,16,17], which is suitable for automatic frequency tuning. However, due to the frequency-splitting in close coupling condition, there may be multiple resonant points, such as the middle resonant point, odd, and even splitting points. The previous self-oscillating methods make the system operate at one of the splitting points, but not always with maximum efficiency [18–20], and some studies indicate that the self-oscillating system becomes unstable under disturbance because it will hop from one splitting point to another when the circuit parameters change [17].

Furthermore, the self-oscillating control cannot always keep the system resonant since the intrinsic delay in the components of the feedback loop can be added up to several hundred ns and makes the TX current lag behind the output voltage of the inverter, not only detuning the system, but also doing harm to the voltage source inverter, especially at high frequency [9,17,21,22]. Though the constant delay could be compensated by the negative hysteresis link [21] and linear network [22], these methods are only useful for the fixed frequency operation rather than the variable frequency operation caused by frequency tuning. The method in [23] achieves self-adaptive delay compensation, but it is only verified in loose coupling and needs deeper research.

To solve the problems mentioned above, in this paper, the self-oscillating frequency and its variation trend with circuit parameter changes are analyzed with different feedback variables. The WPT system is modeled as a non-linear switched system, and the Hamel locus is applied since it is precise and intuitive in the prediction of self-oscillating frequency and its variation trend, and is easy in modelling the delay link [21,24]. The series-series (SS) topology WPT system is chosen as an example because the resonant frequency in the SS topology is independent of the load and the coupling coefficient [12,18]. The TX current and RX current are treated as the self-oscillating feedback variables to analyze the self-oscillating characteristics, and the RX current is chosen for feedback because the system operates steadily in the middle resonant frequency with the maximum efficiency, regardless of the frequency splitting. On the basis of analysis of the variation trend between the self-oscillating frequency and the delay in the feedback loop, a novel automatic frequency tuning with automatic delay compensation is proposed, in which only frequency measurement and delay setting are needed. Furthermore, to realize the automatic frequency tuning, a function of the detuning and the phase difference between the currents in TX and RX is also investigated, and the circuit parameter tuning with the phase difference detection and capacitance adjustment is proposed to realize the synchronous tuning. The experiments verify the effectiveness and robustness of the synchronous tuning method.

2. Analysis of the Self-Oscillating Feedback Methods

The self-oscillating frequency characteristics, using the TX current i_1 or the RX current i_2 as the feedback variable, are analyzed respectively. The power circuit and its linear equivalent circuit of the WPT system are shown in Figure 2a,b, respectively, and the block diagram for control is shown in Figure 3.

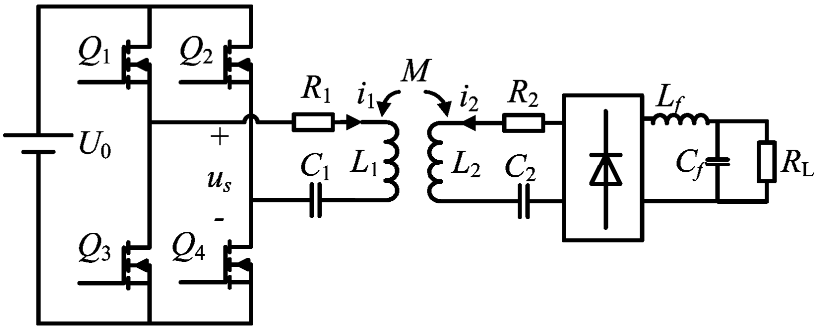

(**a**)

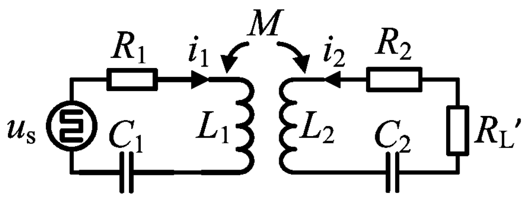

(**b**)

Figure 2. Power circuit and linear equivalent circuit of wireless power transfer (WPT) system: (**a**) power circuit; and (**b**) linear equivalent circuit.

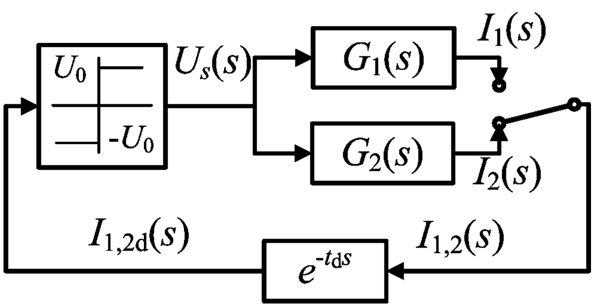

Figure 3. Block diagram of control system.

The power circuit of the WPT system consists of the DC power source, inverter, resonant tanks, rectifier, filter, and load. The DC power source U_0 and the high-frequency inverter composed of MOSFETs Q_1–Q_4 are modeled as a square wave source in Figure 2b. The resonant tanks contains the coils with the inductances L_1, L_2, the capacitors with the capacitances C_1, C_2, and the two equivalent resistors, whose resistance R_1 in the TX, is the sum of resistances of the source, inverter, and TX coil, and the resistance R_2 in the RX is the sum of resistances of the RX coil, rectifier, and filter. The rectifier, filter L_f, C_f, and load R_L can be equivalent to R_L' in Figure 2b, where $R_\mathrm{L}' = (8/\pi^2)R_\mathrm{L}$ [12,25]. M is the mutual inductance, $M = k\sqrt{L_1 L_2}$, and k is the coefficient of mutual inductance.

In Figure 3, the inverter is modeled as an ideal relay link because the dead time in SiC MOSFETs is only several ns and, therefore, ignorable. In order to analyze the frequency characteristics with the feedback variables i_1 or i_2, the Hamel locus functions $H_1(f)$ and $H_2(f)$ without the delay $e^{-t_d s}$are derived.

The transfer functions $G_1(s)$ and $G_2(s)$ can be obtained by solving the complex frequency domain Equation (1) describing the linear part. For the convenience, the circuit parameters of the system is set to symmetrical [25], i.e., $R = R_1 = R_2 + R_\mathrm{L}'$, $L = L_1 = L_2$, $C = C_1 = C_2$ in (2).

$$\begin{cases} I_1(s)\left(R_1 + sL_1 + \frac{1}{sC_1}\right) - I_2(s)\,sM = U_s(s) \\ -I_1(s)\,sM + I_2(s)\left(R_2 + R_L + sL_2 + \frac{1}{sC_2}\right) = 0 \end{cases} \tag{1}$$

$$\begin{cases} G_1(s) = \frac{I_1(s)}{U_s(s)} = \frac{LC^2s^3 + RC^2s^2 + Cs}{s^4(C^2L^2 - C^2M^2) + 2C^2LRs^3 + s^2(C^2R^2 + 2LC) + 2CRs + 1} \\ G_2(s) = \frac{I_2(s)}{U_s(s)} = \frac{C^2Ms^3}{s^4(C^2L^2 - C^2M^2) + 2C^2LRs^3 + s^2(C^2R^2 + 2LC) + 2CRs + 1} \end{cases} \tag{2}$$

The step response of Equation (2) is:

$$q_{1,2}(t) = a_1 \sin(\omega_1 t)\, e^{-b_1 t} \pm a_2 \sin(\omega_2 t)\, e^{-b_2 t} \tag{3}$$

where the sign "$\pm$" is "+" in $q_1(t)$ and "$-$" in $q_2(t)$, and:

$$\begin{cases} a_1 = \frac{1}{(-R^2 + 4(L-M)/C)^{1/2}} & b_1 = \frac{R}{2(L-M)} & \omega_1 = \frac{(-R^2 + 4(L-M)/C)^{1/2}}{2(L-M)} \\ a_2 = \frac{1}{(-R^2 + 4(L+M)/C)^{1/2}} & b_2 = \frac{R}{2(L+M)} & \omega_2 = \frac{(-R^2 + 4(L+M)/C)^{1/2}}{2(L+M)} \end{cases} \tag{4}$$

It can be seen from Equation (4) that the step responses of i_1 and i_2 are the superposition of two exponentially-decayed sinusoidal functions.

The square wave responses $i_1(t)$ and $i_2(t)$ are the superposition of a series of positive and negative step responses $q_1(t)$ and $q_2(t)$, as shown in (5), and the derivatives $\mathrm{d}i_1(t)/\mathrm{d}t$ and $\mathrm{d}i_2(t)/\mathrm{d}t$ are given in (6):

$$\begin{aligned} i_{1,2}(t) &= 2U_0\left(\sum_{n=1}^{\infty} q_{1,2}(t + nT) - \sum_{n=2}^{\infty} q_{1,2}\left(t - \frac{T}{2} + nT\right)\right) \\ &= a_1U_0\frac{e^{-b_1t}\sin\omega_1\left(t - \frac{1}{2}T\right) + e^{-b_1\left(t - \frac{1}{2}T\right)}\sin\omega_1 t}{\cosh\frac{b_1T}{2} + \cos\frac{\omega_1T}{2}} \pm a_2U_0\frac{e^{-b_2t}\sin\omega_2\left(t - \frac{1}{2}T\right) + e^{-b_2\left(t - \frac{1}{2}T\right)}\sin\omega_2 t}{\cosh\frac{b_2T}{2} + \cos\frac{\omega_2T}{2}} \quad t \in \left(0, \frac{T}{2}\right] \end{aligned} \tag{5}$$

$$\begin{aligned} \frac{di_{1,2}(t)}{dt} &= a_1U_0\frac{\left(-b_1e^{-b_1t}\sin\omega_1\left(t - \frac{1}{2}T\right) + \omega_1e^{-b_1t}\cos\omega_1\left(t - \frac{1}{2}T\right) - b_1e^{-b_1\left(t - \frac{1}{2}T\right)}\sin\omega_1 \mathrm{t} + \omega_1e^{-b_1\left(t - \frac{1}{2}T\right)}\cos\omega_1 \mathrm{t}\right)}{\cosh\frac{b_1T}{2} + \cos\frac{\omega_1T}{2}} \quad t \in \left(0, \frac{T}{2}\right] \\ &\pm a_2U_0\frac{\left(-b_1e^{-b_2t}\sin\omega_2\left(t - \frac{1}{2}T\right) + \omega_2e^{-b_2t}\cos\omega_2\left(t - \frac{1}{2}T\right) - b_2e^{-b_2\left(t - \frac{1}{2}T\right)}\sin\omega_2 \mathrm{t} + \omega_2e^{b_2\left(t - \frac{1}{2}T\right)}\cos\omega_2 \mathrm{t}\right)}{\cosh\frac{b_2T}{2} + \cos\frac{\omega_2T}{2}} \end{aligned} \tag{6}$$

Substituting the period fixed point $t = T/2 = 1/2f$ into (5) and (6) gives the frequency characteristics of i_1, i_2, i.e., the Hamel locus functions, and their derivatives:

$$H_{1,2}(f) = i_{1,2}\left(\frac{1}{2f}\right) = a_1U_0\frac{\sin\frac{\omega_1}{2f}}{\cosh\frac{b_1}{2f}+\cos\frac{\omega_1}{2f}} \pm a_2U_0\frac{\sin\frac{\omega_2}{2f}}{\cosh\frac{b_2}{2f}+\cos\frac{\omega_2}{2f}} \tag{7}$$

$$H\prime_{1,2}(f) = \frac{di_{1,2}\left(\frac{1}{2f}\right)}{dt} = a_1U_0\frac{\omega_1 e^{-\frac{b_1}{2f}} - b_1\sin\frac{\omega_1}{2f}+\omega_1\cos\frac{\omega_1}{2f}}{\cosh\frac{b_1}{2f}+\cos\frac{\omega_1}{2f}} \pm a_2U_0\frac{\omega_2 e^{-\frac{b_2}{2f}} - b_2\sin\frac{\omega_2}{2f}+\omega_2\cos\frac{\omega_2}{2f}}{\cosh\frac{b_2}{2f}+\cos\frac{\omega_2}{2f}} \tag{8}$$

The Hamel loci with the feedback variables i_1 and i_2 are shown in Figure 4a,b respectively, where U_0 = 20 V, R = 3 Ω, L = 50 μH, C = 1750 pF, k = 0.056, and the resonant frequency f_{res} = 538.04 kHz. The system under the chosen frequency is suitable for full bridge inverters, and the close coupling condition k^2Q^2 = 17.857 > 1 is satisfied [20,25]. The frequency range in the loci is $0.5f_{res}$–$2f_{res}$. The arrows in Figure 4 indicate the direction of the frequency increase. The intersections of the negative x-axis and the loci are self-oscillating points, and among them the ones crossing from the negative to positive are stable ones, while the others are unstable ones [21,24].

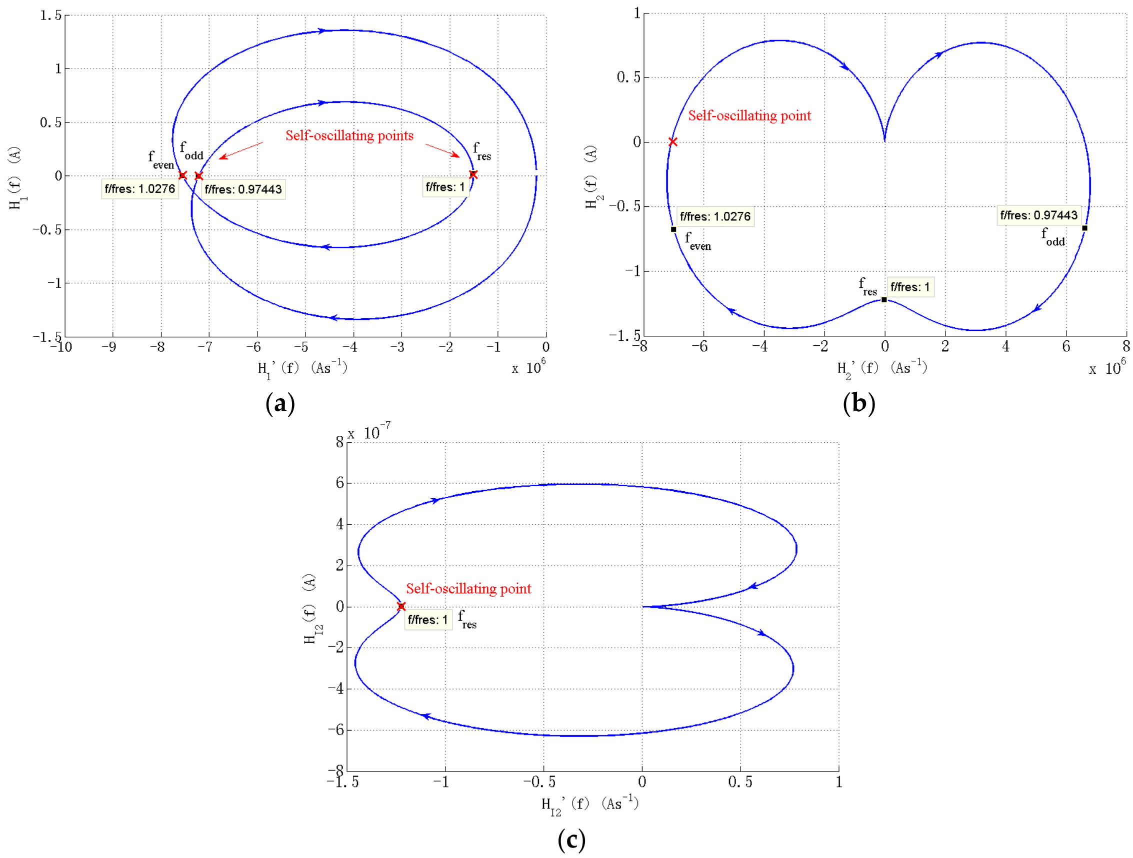

Figure 4. Hamel loci of different feedback methods: (**a**) feedback variable i_1; (**b**) feedback variable i_2; and (**c**) feedback variable i_2 with an integrator.

For the feedback variable i_1, the inverter flips when i_1 crosses zero, so the self-oscillating points are in coincidence with the middle resonant point or the splitting points, as shown in Figure 4a. Unfortunately, the middle resonant point with the frequency f_{res} is unstable, and both of the odd and even splitting points [26] with the splitting frequencies f_{odd} and f_{even} are stable. Studies in [18–20] indicate that, in the close coupling 2-coil WPT systems, though the power at f_{res} is smaller than the one at f_{odd} or f_{even}, the efficiency is higher at f_{res}. The reason why the efficiency is more important than power is that the high power can be easily obtained by high voltage source.

For the feedback variable i_2, the inverter flips when i_2 crosses zero, so the self-oscillating point is not equal to the middle resonant point or the splitting points because of the phase difference between i_1 and i_2, as shown in Figure 4b. The middle resonant point, however, is located at the intersection between the loci and the negative y-axis, and can be shifted to the negative x-axis by adding an integrator in $G_2(s)$ to yield 90° phase shift, as shown in Figure 4c.

The circuit parameters disturbance occurs when the inductances and the capacitances of the resonant tanks change in the varying environment. The self-oscillating characteristics under parameters disturbance are analyzed by plotting the Hamel loci of the system with asymmetric parameters. Without loss of generality, the variation in C_2 represents the detuning. The explicit Hamel locus functions are difficult to derive, so the Symbolic Math Toolbox of the MATLAB is used. Figure 5a,b shows the Hamel loci for the feedback variables i_1 and i_2, respectively, with the C_2 increased to 1900 pF. An integrator is added in Figure 5b to produce a 90° phase shift. In Figure 5a, there is only one stable self-oscillating point rather than two, as in Figure 4a, and this point is in the vicinity of the even splitting point. Thus, if the system operates at the odd splitting point originally, this circuit parameter disturbance will make the system go into the even splitting point after being retuned, which means the robustness for the feedback variable i_1 is low. While in Figure 5b, there is only one stable self-oscillating point when detuning, so the system goes back to the middle resonant point after being retuned. As a result, i_2 is more suitable for feedback.

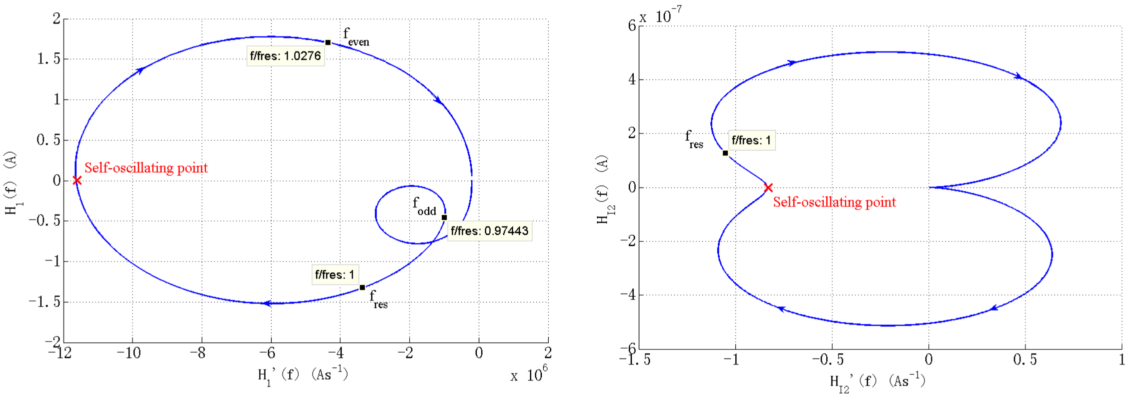

(**a**) (**b**)

Figure 5. Hamel loci when C_2 increases: (**a**) feedback variable i_1; and (**b**) feedback variable i_2 with an integrator.

3. Automatic Delay Compensation in Self-Oscillating WPT System

The frequency characteristics and delay compensation of the self-oscillating WPT system with the delay $e^{-t_d s}$are analyzed in this section. The transfer functions of i_1 and i_2 with the delay are:

$$G_{d1,2}(s) = G_{1,2}(s)\, e^{-t_d s} \tag{9}$$

The Hamel locus function $H_{d1,2}(f)$ with the delay are obtained by derivation similar to Equations (3)–(7). The implicit function (Equation (10)) of the delay t_d and the self-oscillating period T is obtained by letting $H_{d1,2}(f) = 0$, and the function is plotted in Figure 6 in the different range of t_d.

$$F_{1,2}(t_d, T) = H_{d1,2}(T/2) = 0 \tag{10}$$

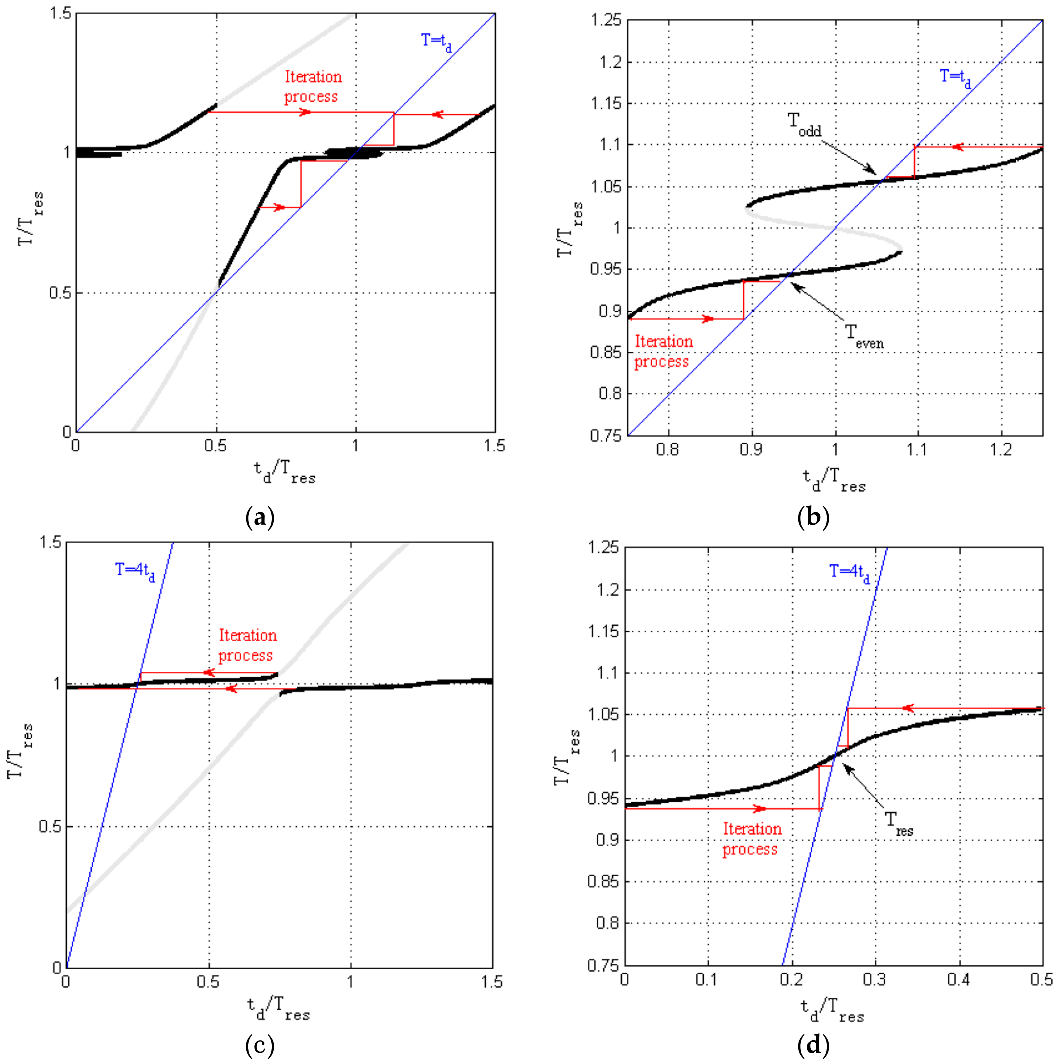

Figure 6. Function $F_{1,2}(t_d,T)$: (**a**) $F_1(t_d,T)$ in full range; (**b**) $F_1(t_d,T)$ in partial range; (**c**) $F_2(t_d,T)$ in full range; and (**d**) $F_2(t_d,T)$ in partial range.

For the feedback variable i_1 shown in Figure 6a,b, all of the deep-colored points in the curve represent the stable self-oscillating points, and the light-colored ones represent the unstable self-oscillating points. In Figure 6b, the upper intersection between the line $T = t_d$ and the stable part of the curve is the odd splitting point, and the lower is the even splitting point, the U_0 lags i_1 by exactly one period at these two points. So the splitting points can be reached by setting $t_d = T$ repeatedly, as in the iteration process shown by the red arrows. The system stabilizes at the odd splitting point with a longer initial delay, and at the even mode point with a shorter initial delay. Similarly, when using i_2 as the feedback variable in Figure 6c,d, the middle resonant point locates at the unique intersection between the line $T = 4t_d$ and the stable part of the curve. Thus, it can be reached by setting $t_d = T/4$ repeatedly, which is equivalent to a 90° phase shift in the feedback loop just like an integrator in Figure 4c. Only 2–3 iterations are needed if the initial delay is in the vicinity of the estimated target values, such as in Figure 6b,d, while more iterations are needed for a large deviated initial delay.

The resonant points can be found in a large frequency range even if the circuit parameters are unknown, so new resonant points can be reached when the parameters varies because the iteration is always in progress. Moreover, the error of the frequency measurement can be limited to the level of 0.002% easily (about 10 Hz, for two decimals in kHz), which is precise enough for the delay setting using controllable delay lines such as the DS1023-500. The precision of the frequency measurement is higher than that of the measurement of the voltage, current or reflected impedance amplitude, and the random error, due to the voltage fluctuation in the amplitude measurement, does not occur in the frequency measurement. This method can also be used on the occasion where the input voltage is unstable because no amplitude is measured, and the measurement and actuator are easy to realize, so the practicability is fairly high.

4. Synchronous Tuning

The purpose of circuit parameter tuning is to keep the resonant frequency of the TX equal to that of the RX all the time, i.e., $f_{\text{res}} = f_{\text{res1}} = f_{\text{res2}}$:

$$\begin{cases} f_{res1} = \frac{1}{2\pi\sqrt{L_1C_1}} \\ f_{res2} = \frac{1}{2\pi\sqrt{L_2C_2}} \end{cases} \tag{11}$$

The frequency tuning here is automatic and affected by the circuit parameter variation during the circuit parameter tuning according to the analysis in Figure 5b. Thus, the function between the detuning and the phase difference of i_1 and i_2 is studied below, and an automatic circuit parameter tuning method with phase difference measurement and capacitance adjustment is proposed based on the function. The capacitor C_1 is chosen for adjustment because powering the actuator in the TX is easier than that in the RX.

Firstly, the frequency characteristic function for the automatic frequency tuning is obtained by setting the delay in the Hamel locus function $H_{d2}(f)$ to $t_d = T/4 = 1/4f$. The capacitance C_1 is treated as an independent variable to derive the relation of C_1 and self-oscillating frequency f as:

$$F_2\left(C_1, f\right) = H_{d2}\left(f\right)\big|_{t_d=T/4} = 0 \tag{12}$$

and the function $f(C_1)$ is obtained by solving (12) and plotted in Figure 7. Substituting $s = j\omega$ in Equation (1) to obtain the Equation (13), and the i_1 and i_2 in the frequency domain can be obtained by solving Equation (13):

$$\begin{cases} \mathbf{I}_1\left(C_1, \omega\right) = I_1\left(s\right)\big|_{s=j\omega} \\ \mathbf{I}_2\left(C_1, \omega\right) = I_2\left(s\right)\big|_{s=j\omega} \end{cases} \tag{13}$$

where C_1 and ω are independent variables, and $\mathbf{I_1}$ and $\mathbf{I_2}$ are the current phasors.

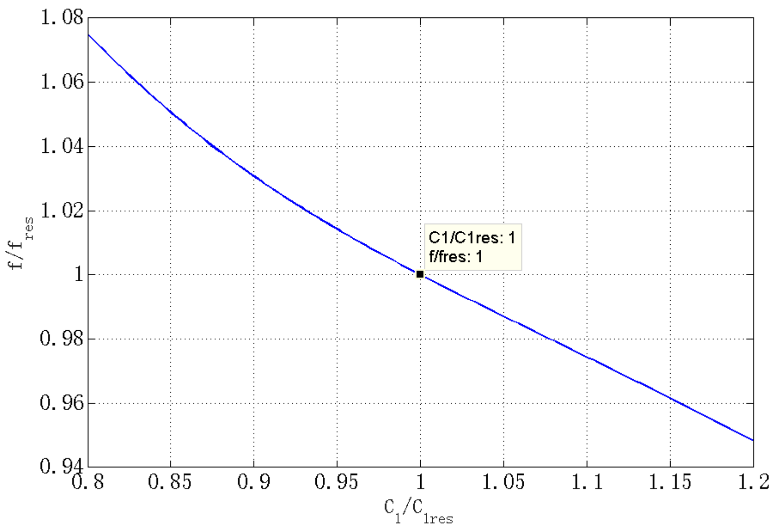

Figure 7. Function $f(C_1)$.

Secondly, substituting the value of C_1 and its corresponding angular frequency $\omega = 2\pi f$ in the $f(C_1)$ in the $i_1(C_1,\omega)$ and $i_2(C_1,\omega)$ to obtain the functions of C_1 and the phase of i_1 and i_2, i.e., $\phi_1(C_1)$, and $\phi_2(C_1)$, and then the phase difference function $\Delta\phi(C_1) = \phi_2(C_1) - \phi_1(C_1)$, as shown in Figure 8.

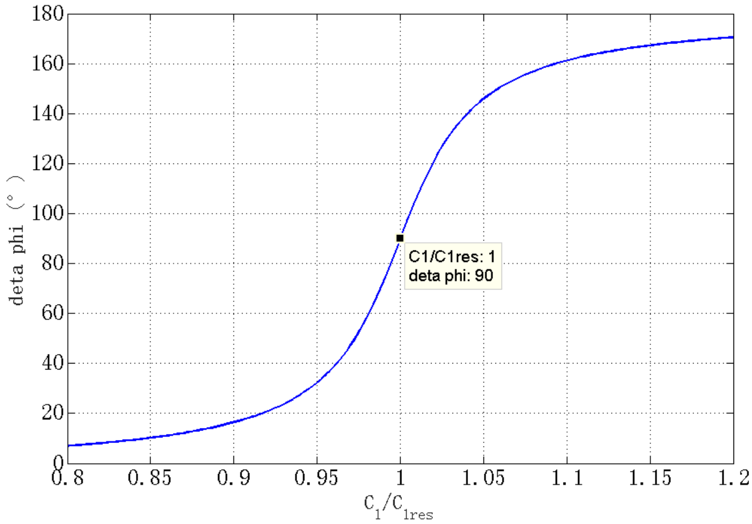

Figure 8. Function $\Delta\phi(C_1)$.

Above all, it is clear that this function is monotonic, and the circuit parameters are tuned only when $\Delta\phi = 90^\circ$. Therefore, the circuit parameter tuning can be realized by the inspection of the $\Delta\phi$ and the adjustment of the C_1 to keep $\Delta\phi = 90^\circ$ within the margin of error.

5. Experimental Verification

The system block diagram and experimental platform are shown in Figures 9 and 10, respectively. The synchronous tuning circuit includes the self-oscillating feedback loop, delay adjustment circuit, and capacitance adjustment circuit. The feedback loops for the feedback variable i_1 and i_2 include the current transformer CT_1, CT_2, zero-crossing comparator ZC_1, ZC_2, controllable delay line, and MOSFET driver. A wireless signal transfer module is needed to meet the demand of the transfer distance and rate in the feedback loop for i_2, such as the fast infrared module HSDL-3602 with the link distance 1.5 m and signal rate 4 Mb/s, or radio frequency module [18] for further transfer distance and with a block between the TX and the RX. The delay adjustment includes the frequency measurement (FM) in the microcontroller unit (MCU) and the controllable delay line. The circuit parameter tuning circuit includes phase detector (PD) in the MCU and a variable capacitor adjusted by a stepper motor. Capacitor arrays or varicap diodes can also be used on different occasions [6,11,12,25]. The components and circuit parameters are listed in Tables 1 and 2, respectively. The high-Q resonant tanks are comprised of copper pipes with large diameter and ceramic plate capacitors with low dielectric loss. The inductances and capacitances are measured by an inductance (L), capacitance (C) and resistance (R) meter (LCR meter) (TH2828, Tonghui Electronic Co. Ltd., Changzhou, Jiangsu, China), the equivalent resistances are measured by dividing the resonant voltage by the resonant current, and the middle resonant frequency, splitting frequency and the intrinsic delay are observed with an oscilloscope (TDS2024B, Tektronix Electronic Co. Ltd., Beaverton, OR, USA). The calculated values of these resonant frequencies are acquired using the measurement values of the components. The delay for the feedback variable $i_{1,2}$ includes the controllable delay t_{dc} and the intrinsic delay $t_{ds1,2}$, i.e., $t_\mathrm{d} = t_{ds1,2} + t_{dc}$, and $t_{ds1,2} = t_{ds\mathrm{A}1,2} + t_{ds\mathrm{B}}$, marked in detail in Figure 9. The required t_d can be acquired by setting $t_{dc} = t_d - t_{ds1,2}$ using the controllable delay line made of two DS1023-500 in cascade, with the delay step of 5 ns. The delays of the $CT_{1,2}$ are far shorter than 5 ns and can be included within the $t_{ds1,2}$ as a constant.

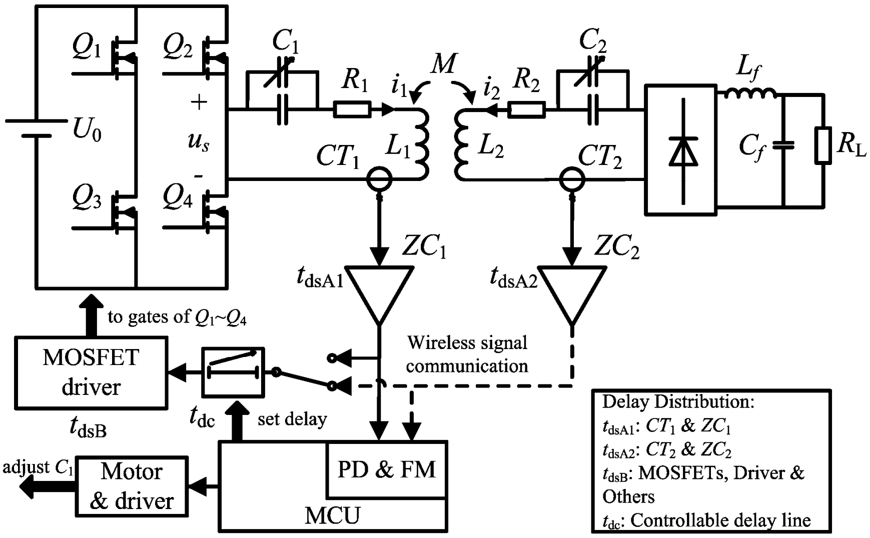

Figure 9. Block diagram of the experimental platform.

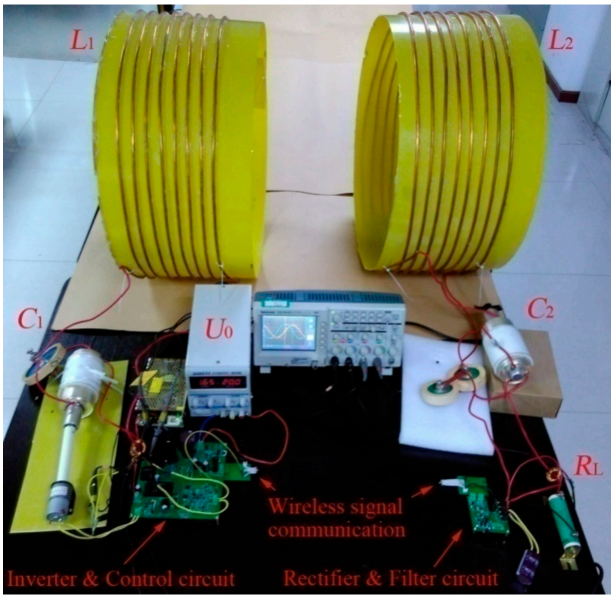

Figure 10. Photo of the experimental platform.

Table 1. Types of components.

Part	Name	Material or Type
Resonant tanks	Coil Fixed capacitor Variable capacitor	Copper pipe Φ = 6 mm Ceramic plate capacitor Vacuums adjustable capacitor
Power circuit	MOSFET MOSFET driver Rectifier diode	SCH2080KE IR2011 MBR3045
Feedback loop	Delay line Comparator Infrared data communication	DS1023-500 MAX913 HSDL-3602
Control circuit	MCU Motor driver	STM32F405RE L298N

Table 2. Parameters of components.

Symbol	Value	Symbol	Value
U_0 (V)	20.0	k	0.056
L_1, L_2 (μH)	49.1, 49.5	t_{ds1}, t_{ds2} (ns)	175, 290
C_1, C_2 (pF)	1774.4, 1759.6	$f_{res}, f_{odd}, f_{even}$ (kHz) (measurement)	539.69, 530.79, 547.98
R_1, R_2, R_L (Ω)	0.73, 0.54, 10.32	$f_{res}, f_{odd}, f_{even}$ (kHz) (calculation)	539.20, 532.63, 546.75

The flow chart of the automatic delay compensation is shown in Figure 11 according to the analysis in Section 3. The estimated value of the initial delay $t_d(0)$ is set to the vicinity of T_{res} for the feedback variable i_1, and to the vicinity of $T_{res}/4$ for the feedback variable i_2 in order to achieve a short stabilization time. The iteration process is shown in Figure 12, and the range of delay, period, and frequency are measured and listed in Table 3. It can be seen that for the feedback variable i_1, the system stabilizes at the odd splitting point under a long initial delay, and at the even splitting point under a short initial delay; and for i_2, the system stabilizes at the middle resonant point regardless of the initial delay. The tuning process is not only fully automatic with the repetitive loop, just as is shown in Figure 1b, but also fast because only 2–3 iterations are needed for i_1, and 1–2 iterations for i_2.

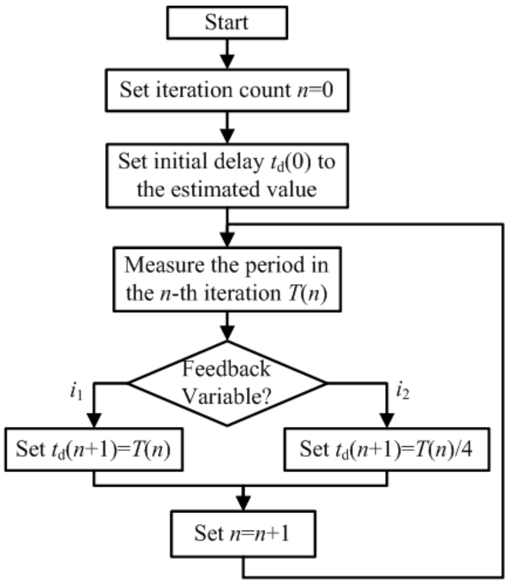

Figure 11. Flow chart of the automatic delay compensation.

The Figure 13 shows the variation tendency of the self-oscillating frequency with C_1 or C_2, for the feedback variable i_1 or i_2, respectively. In Figure 13a, for the feedback variable i_1, the system is initially tuned in the odd splitting point. When C_1 increases from the tuned value C_{1res} to a certain amount, the frequency will hop to the vicinity of the even mode, and the frequency is tuned to the even mode when C_1 decreases to C_{1res} again, as shown in the track ABCDE. The track EFGHA shows the frequency hopping from the even to odd splitting point. The similar frequency variation process with the change of C_2 is shown in Figure 13b, while in Figure 13c,d, for the feedback variable i_2, the system always goes back to the middle resonant point after the C_1 or C_2 is retuned, so the robustness for i_2 is stronger. The variation trends of the self-oscillating frequency in the experiments are in good agreement with the analysis in Section 2, and the transfer power and efficiency shown in Table 4 indicate that though the power is lower, the efficiency is higher at the middle resonant point.

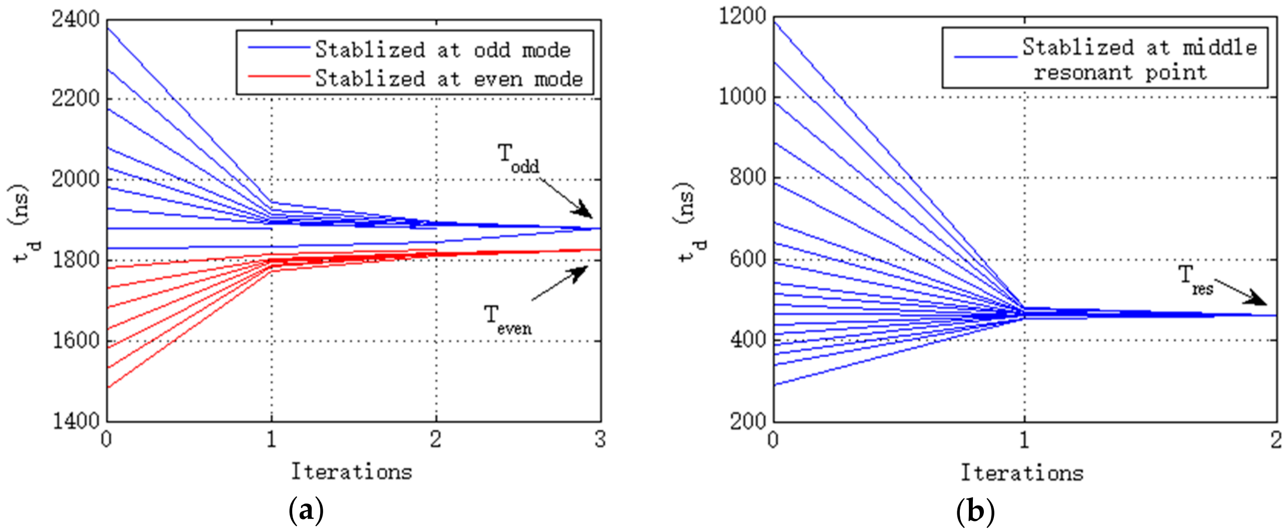

Figure 12. The iteration process of t_d with different feedback variables, at different initial delay: (**a**) feedback variable i_1; and (**b**) feedback variable i_2.

Table 3. Range of delay, period, and frequency in each step of the delay compensation.

Iteration Count n	Feedback Variable i_1 (Odd Splitting Frequency)			Feedback Variable i_1 (Even Splitting Frequency)			Feedback Variable i_2		
	t_d (ns)	T (ns)	f (kHz)	t_d (ns)	T (ns)	f (kHz)	t_d (ns)	T (ns)	f (kHz)
0	1830–2380	1837.06–1947.55	544.34–513.46	1480–1780	1778.13–1813.32	562.39–551.48	290–1190	1823.96–1921.01	548.26–520.56
1	1835–1945	1847.47–1897.11	541.28–527.11	1775–1815	1811.53–1823.81	552.01–548.30	455–480	1850.85–1849.68	540.29–540.63
2	1845–1895	1877.66–1882.28	532.57–531.27	1810–1825	1823.65–1824.88	548.35–547.98	460	1852.92	539.69
3	1880	1883.98	530.79	1825	1824.88	547.98			

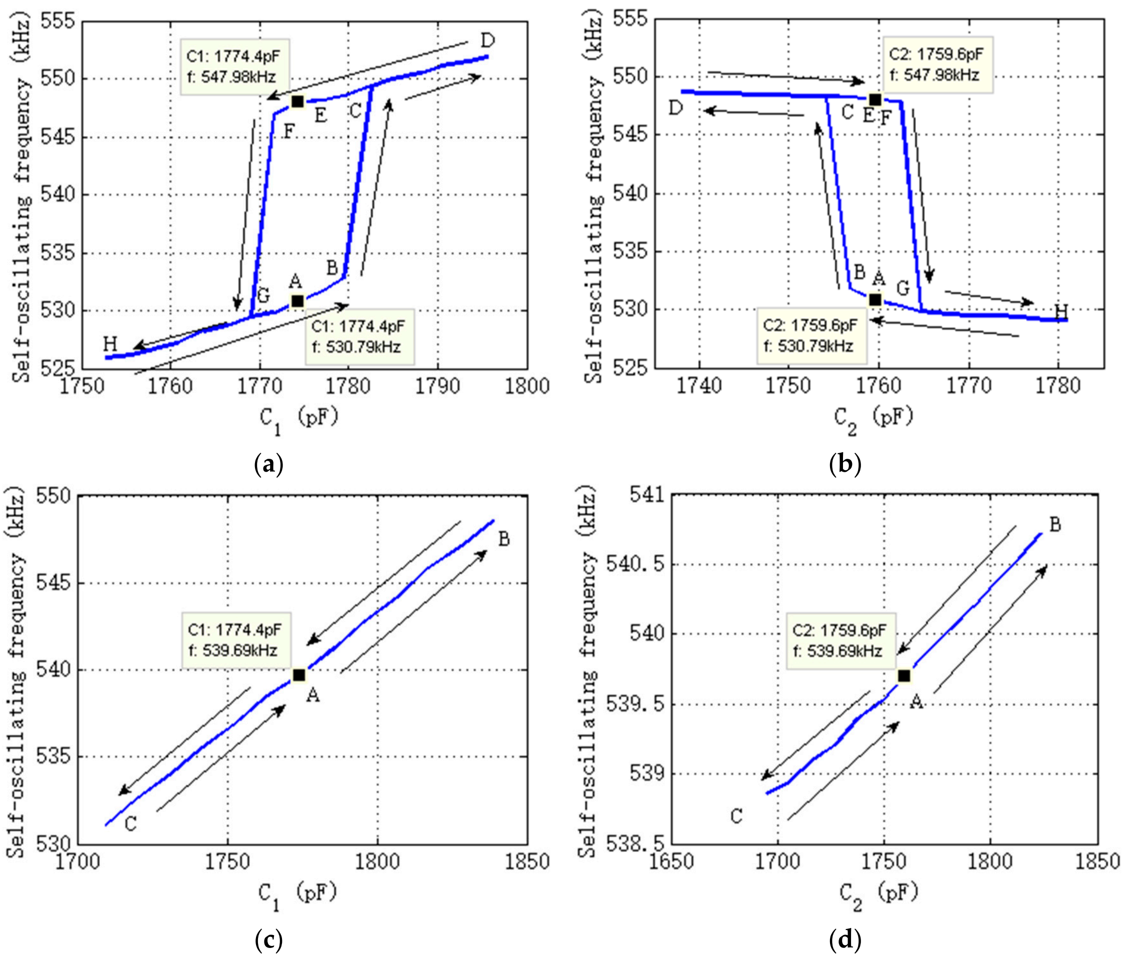

Figure 13. Variation trends of self-oscillating frequency in different feedback mode. (**a**) Feedback variable i_1, adjust C_1; (**b**) feedback variable i_1, adjust C_2; (**c**) feedback variable i_2, adjust C_1; and (**d**) feedback variable i_2, adjust C_2.

Table 4. Measurement results of power and efficiency.

Feedback Variable	i_1 (Odd Splitting Point)	i_1 (Even Splitting Point)	i_2
Power (W)	37.0	36.8	30.2
Efficiency (%)	83.5	83.8	87.2

The waveforms of u_s, i_1, and i_2 for the automatic circuit parameter tuning are shown in Figure 14. The current values are obtained by measuring the voltage across the sampling resistor in the current transformer and displayed as the voltage value in the oscilloscope. In Figure 14a, C_2 is set to 1823.6 pF, which is 64.0 pF larger than that of the original resonant value to represent the circuit parameter tuning, and the phase different of i_1 and i_2 is far less than 90°. Thus, the new resonant value of C_1 needs to be increased according to the analysis in Figure 8. In Figure 14b–d, the phase difference approaches to 90° gradually, and finally comes into the range of 90° $\pm$ 1°. The frequency detuning exists for a short time, but disappears after the automatic circuit parameter tuning. The amplitude of i_2 almost remains constant in the process, indicating that the received power is stable in a certain range of detuning during the tuning process.

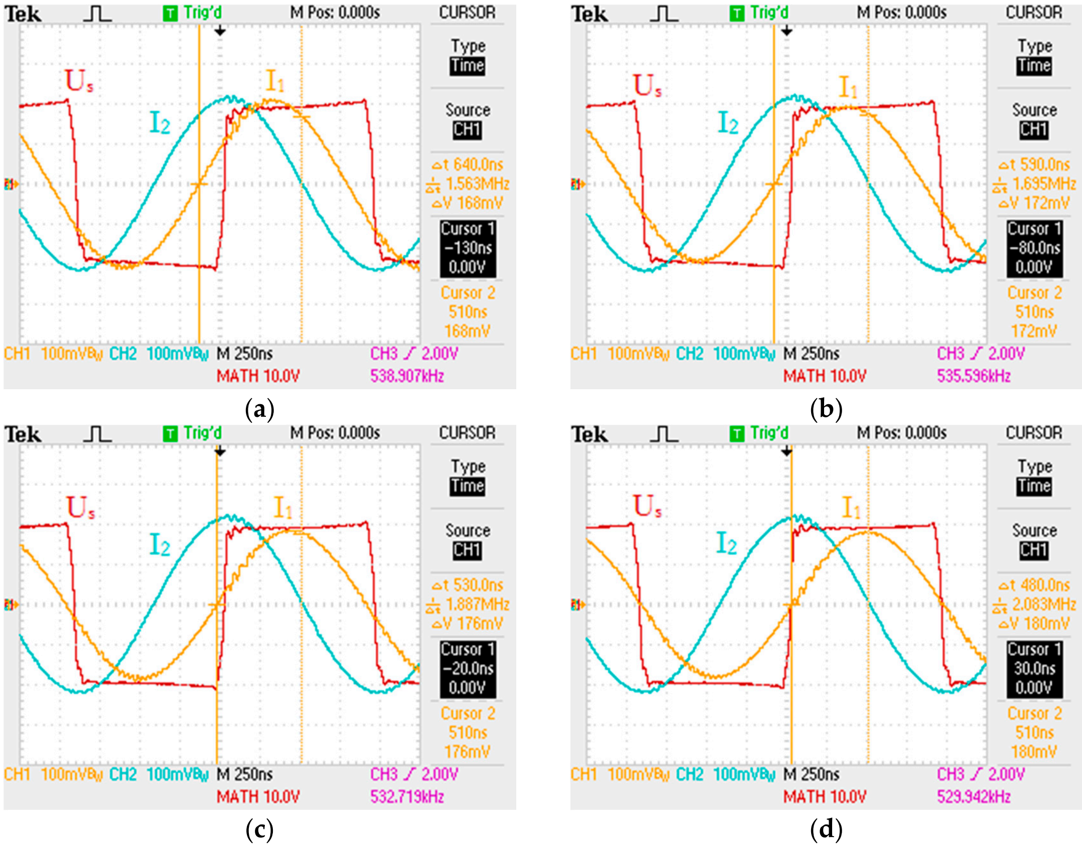

Figure 14. Waveforms of the voltage u_s of the inverter, and the currents i_1 and i_2 in the TX and RX during the circuit parameter tuning process. (**a**) C_1 = 1774.4 pF, Δϕ = 56.4°; (**b**) C_1 = 1794.9 pF, Δϕ = 65.9°; (**c**) C_1 = 1816.5 pF, Δϕ = 80.2°; and (**d**) C_1 = 1838.7 pF, Δϕ = 89.4°.

6. Conclusions

The self-oscillating characteristics of a close-coupling WPT system for the feedback variables TX current and RX current are analyzed. It is proved by both theory and experiments that the system operates more stably and efficiently at the middle resonant point for the feedback variable RX current than at the odd or even splitting point for the feedback variable TX current, and the frequency-hopping caused by the frequency-splitting is eliminated. The detuning due to the intrinsic delay are solved by the automatic delay compensation with the iteration of delay and period, and the detuning due to the circuit parameter variation are solved by the automatic circuit parameter tuning with the function of detuning and phase difference. The frequency and circuit parameter tuning can be used at the same time to realize the synchronous tuning. The tuning is fully automatic and precise, and is suitable for practical applications where circuit parameter values are easy to change.

The proposed frequency and circuit parameter tuning can be used not only in WPT systems, but also in other applications using high frequency resonant inverters, such as inductive heating or electronic ballast. Using the Hamel locus to analyze the frequency characteristic and the circuit parameter influence can also be popularized to the related areas.

Acknowledgments: The research was supported by the Experimental teaching and research center in the School of Electrical Engineering, Wuhan University.

Author Contributions: Po Hu modeled the system and revised the paper; Jieshuai Ren researched the synchronous tuning method and wrote the initial draft; Jieshuai Ren and Wenan Li established the experimental platform, conducted the experiments and analyzed the experimental data.

Conflicts of Interest: The authors declare no conflict of interest.

Abbreviations

The following abbreviations are used in this manuscript:

WPT	Wireless power transfer
TX	Transmitter
RX	Receiver
SS	Series-series
MOSFET	Metal-Oxide-Semiconductor Field Effect Transistor
MCU	Micro programmed Control Unit
LCR meter	Inductance (L), capacitance (C) and resistance (R) meter

References

1. Sample, A.P.; Meyer, D.A.; Smith, J.R. Analysis, Experimental Results, and Range Adaptation of Magnetically Coupled Resonators for Wireless Power Transfer. *IEEE Trans. Ind. Electron.* **2011**, *58*, 544–554. [CrossRef]
2. Brusamarello, V.J.; Blauth, Y.B.; Azambuja, R.; Mueller, I. A Study on Inductive Power Transfer with Wireless Tuning. In Proceedings of the IEEE Instrumentation and Measurement Technology Conference, Graz, Austria, 13–16 May 2012; pp. 1098–1103.
3. Li, Q.; Liang, Y.C. An Inductive Power Transfer System with a High-Q Resonant Tank for Mobile Device Charging. *IEEE Trans. Power Electron.* **2015**, *30*, 6203–6212. [CrossRef]
4. Moorey, C.; Holderbaum, W.; Potter, B. Investigation of High-Efficiency Wireless Power Transfer Criteria of Resonantly-Coupled Loops and Dipoles through Analysis of the Figure of Merit. *Energies* **2015**, *8*, 11342–11362. [CrossRef]
5. Kurs, A.; Karalis, A.; Moffatt, R.; Joannopoulos, J.D.; Fisher, P.; Soljacic, M. Wireless Power Transfer via Strongly Coupled Magnetic Resonances. *Science* **2007**, *317*, 83–86. [CrossRef] [PubMed]
6. Thuc, P.D.; Lee, J. A Dynamically Adaptable Impedance-Matching System for Midrange Wireless Power Transfer with Misalignment. *Energies* **2015**, *8*, 7593–7617.
7. Zhang, Y.; Lu, T.; Zhao, Z.; He, F.; Chen, K.; Yuan, L. Employing Load Coils for Multiple Loads of Resonant Wireless Power Transfer. *IEEE Trans. Power Electron.* **2015**, *30*, 6174–6181. [CrossRef]
8. Johari, R.; Krogmeier, J.V.; Love, D.J. Analysis and Practical Considerations in Implementing Multiple Transmitters for Wireless Power Transfer via Coupled Magnetic Resonance. *IEEE Trans. Ind. Electron.* **2014**, *61*, 1774–1783. [CrossRef]
9. Dai, X.; Sun, Y. An Accurate Frequency Tracking Method Based on Short Current Detection for Inductive Power Transfer System. *IEEE Trans. Ind. Electron.* **2014**, *61*, 776–783. [CrossRef]
10. Wang, J.; Zhu, Z.; Li, C.; Huangfu, J.; Ran, L. PLL-Based Self-Adaptive Resonance Tuning for a Wireless-Powered Potentiometer. *IEEE Trans. Circuits Syst. II* **2013**, *60*, 392–396. [CrossRef]
11. Kim, J.; Jeong, J. Range-Adaptive Wireless Power Transfer Using Multiloop and Tunable Matching Techniques. *IEEE Trans. Ind. Electron.* **2015**, *62*, 6233–6241. [CrossRef]
12. Bac, X.N.; Vilathgamuwa, D.M.; Foo, G.H.B.; Wang, P.; Ong, A.; Madawala, U.K.; Trong, D.N. An Efficiency Optimization Scheme for Bidirectional Inductive Power Transfer Systems. *IEEE Trans. Power Electron.* **2015**, *30*, 6310–6319.
13. Wang, B.; Hu, A.P.; Budgett, D. Maintaining middle zero voltage switching operation of parallel-parallel tuned wireless power transfer system under bifurcation. *IET Power Electron.* **2014**, *7*, 78–84. [CrossRef]
14. Gao, Y.; Farley, K.; Tse, Z. A Uniform Voltage Gain Control for Alignment Robustness in Wireless EV Charging. *Energies* **2015**, *8*, 8355–8370. [CrossRef]
15. Teck, C.B.; Kato, M.; Imura, T.; Sehoon, O.; Hori, Y. Automated Impedance Matching System for Robust Wireless Power Transfer via Magnetic Resonance Coupling. *IEEE Trans. Ind. Electron.* **2013**, *60*, 3689–3698.
16. Ziaie, B.; Rose, S.C.; Nardin, M.D.; Najafi, K. A Self-Oscillating Detuning-Insensitive Class-E Transmitter for Implantable Microsystems. *IEEE Trans. Biomed. Eng.* **2001**, *48*, 397–400. [CrossRef] [PubMed]
17. Tang, C.; Sun, Y.; Dai, X.; Wang, Z.; Su, Y.; Hu, A. Transition control of bifurcated frequencies in inductive power transfer systems through time delay perturbation. *Acta Phys. Sin.-Chin. Ed.* **2013**, *62*, 508–517. (In Chinese)
18. Li, H.; Li, J.; Wang, K.; Chen, W.; Yang, X. A Maximum Efficiency Point Tracking Control Scheme for Wireless Power Transfer Systems Using Magnetic Resonant Coupling. *IEEE Trans. Power Electron.* **2015**, *30*, 3998–4008. [CrossRef]

19. Zhang, Y.; Zhao, Z. Frequency Splitting Analysis of Two-Coil Resonant Wireless Power Transfer. *IEEE Antennas Wirel. Propag. Lett.* **2014**, *13*, 400–402. [CrossRef]
20. Huang, R.; Zhang, B.; Qiu, D.; Zhang, Y. Frequency Splitting Phenomena of Magnetic Resonant Coupling Wireless Power Transfer. *IEEE Trans. Magn.* **2014**, *50*, 1–4. [CrossRef]
21. Williams, D.; Bingham, C.; Foster, M.; Stone, D. Hamel locus design of self-oscillating DC-DC resonant converters. *IET Power Electron.* **2010**, *3*, 86–94. [CrossRef]
22. Yan, K.; Chen, Q.; Hou, J.; Ren, X.; Ruan, X. Self-Oscillating Contactless Resonant Converter with Phase Detection Contactless Current Transformer. *IEEE Trans. Power Electron.* **2014**, *29*, 4438–4449. [CrossRef]
23. Ren, J.; Hu, P.; Yang, D.; Liu, D. Tuning of Mid-Range Wireless Power Transfer System Based on Delay-Iteration Method. *IET Power Electron.* **2016**, *9*, 1563–1570. [CrossRef]
24. Gille, J.C.; Pelegrin, M.J.; Decaulne, P. *Feedback Control Systems: Analysis, Synthesis, and Design*; McGraw-Hill: New York, NY, USA, 1959; pp. 446–462.
25. Colak, K.; Asa, E.; Bojarski, M.; Czarkowski, D.; Onar, O.C. A Novel Phase-Shift Control of Semibridgeless Active Rectifier for Wireless Power Transfer. *IEEE Trans. Power Electron.* **2015**, *30*, 6288–6297. [CrossRef]
26. Niu, W.; Chu, J.; Gu, W.; Shen, A. Exact Analysis of Frequency Splitting Phenomena of Contactless Power Transfer Systems. *IEEE Trans. Circuits Syst. I Regul. Pap.* **2013**, *60*, 1670–1677. [CrossRef]